An Effective Integration of APM and OBC With Simultaneous Operation and Entire ZVS Range for Electric Vehicle

Gibum Yu, *Student Member, IEEE*, and Sewan Choi, *Fellow, IEEE*

***Abstract*—This article proposes an effective integration of APM and OBC providing simultaneous operation without an extra circuit and entire ZVS range of all switches. The integrated circuit of the proposed charger is configured by combining high voltage-side switch legs of the LLC resonant converter of OBC and the PSFB converter of APM. In the simultaneous mode, by operating the common leg as a lagging leg of the phase-shift full bridge (PSFB) converter, the conduction losses of the common leg switches are decreased due to current cancellation effect, and the lagging leg switches of the PSFB converter achieve entire ZVS operation. Further, in the APM standalone mode, entire ZVS operation of the lagging leg switches is also secured by utilizing the magnetizing current of the LLC resonant converter. As a result, the proposed integrated charger achieves comprehensive improvement in terms of efficiency as well as volume and cost. A laboratory prototype combining a 3.7-kW LLC resonant converter with a 1-kW PSFB converter is built and tested in order to verify the performance and theoretical claims.**

***Index Terms*—High efficiency, integrated electric vehicle (EV) charger, LLC resonant converter, phase-shift full bridge (PSFB) converter, soft switching, variable dc-link control.**

I. Introduction

THE market size of power conversion units in electric vehicles (EVs), such as on-board battery chargers (OBCs) and auxiliary power modules (APMs), will be proportional to growth of EV sales (2.1 Million units in 2019)[1], [2]. Fig. 1 shows the schematic diagram of a typical EV power train. OBC [3]–[8] charges the high-voltage (HV) battery wherever there is an electric power outlet available, and APM [9]–[13] charges the low-voltage (LV) battery for auxiliary loads, such as audio, instrument panel, and navigation system. Furthermore, during OBC operation, communication with the battery control module, instrument panel, and mobile devices is required, which can drain the LV battery. Therefore, APM should provide a continuous power of usually lower than 400 W during OBC operation [14].

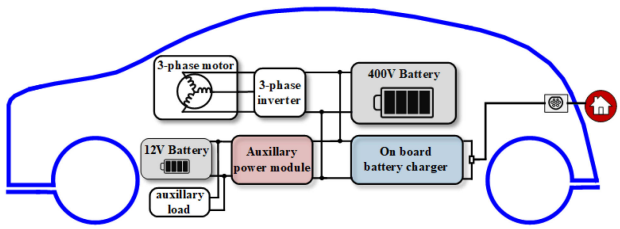

Fig. 1. Schematic diagram of typical EV power train.

Due to the increasing demand for driving range extension of EVs, HV battery capacities have been increasing. As the HV battery capacity increases, the high-power OBC demand increases to minimize charging time. The power level of the OBC is mostly 3.3 or 6.6 kW at present time, but it will increase to 11 and 22 kW, or even higher [15]. Although the power level of the APM is currently in the range of 1–2 kW, new auxiliary loads, such as cameras, radars, and light detection for autonomous system in EV, also increase the power level of the APM up to 3–4 kW [16]. Increasing power level of OBC and APM requires high-power density due to limited space of EVs and leads to additional cost and power losses. In order to fulfill these requirements, the U.S. Department of Energy (DoE) sets targets of power density (4.6 kW/L), cost (35–40$/kW), and efficiency (98%) for OBC and APM in 2025 [17].

Integrated chargers that combine two independent functionalities using the same components provide improvement of power density and cost. The most popular concept is integration of traction inverter and OBC [18], [19]. However, it requires the special motor design and decreases the reliability due to motor lifetime reduction by propulsion stress and common mode leakage current. Also, integration of bidirectional dc–dc converter and OBC [20], [21] reduces reliability due to nonisolation between the HV battery and grid. Integration of OBC and APM could improve reliability, power density, and cost by sharing the components, which has been implemented with a package integration [22] or a topology integration [23]–[33]. Basically, the package integration [22] places OBC and APM to the same package, while sharing the cooling system and the housing. The topology integration has been addressed based on two kinds of methods—switch integration method [23]–[29] and transformer

Manuscript received October 9, 2020; revised December 28, 2020; accepted January 27, 2021. Date of publication March 4, 2021; date of current version June 1, 2021. This work was supported by the Korea Government (MSIT) through the National Research Foundation of Korea (NRF) under Grant 2020R1A2C2006301. Recommended for publication by Associate Editor W. Cao. *(Corresponding author: Sewan Choi.)*

The authors are with the Department of Electrical and Information Engineering, Seoul National University of Science and Technology, Seoul 139-743, South Korea (e-mail: kibum7583@seoultech.ac.kr; schoi@seoultech.ac.kr).

Color versions of one or more of the figures in this paper are available online at http://ieeexplore.ieee.org.

Digital Object Identifier 10.1109/TPEL.2021.3063931

integration method [30]–[33], which is more effective compared to the package integration. The integrated chargers in [23] and [24] share full-bridge switches of the ac–dc converter of the OBC with primary switches of the APM. However, the OBC and the APM cannot operate simultaneously due to different switching methods of the common switches in each operation. Further, the APM operation has low efficiency due to the 2-stage power process. The integrated charger in [26] and [27] utilizes the HV switches of the APM as a power decoupling circuit for the OBC. However, the OBC and the APM cannot operate simultaneously, and extra relays are required for mode change. The integrated charger in [30]–[33] combines the OBC and the APM by using a multiwinding transformer. However, the multiwinding transformer has complex design for series leakage inductance value and requires high height. Also, additional buck converter is required in LV side of the APM for simultaneous operation in [31], which reduces the overall efficiency due to high conduction loss and double switching frequency of the buck switch. The integrated charger in [32] employs the CLLLC and LLC resonant converters based on switching frequency control for the OBC and the APM, respectively. Because operating switching frequencies for CLLLC and LLC resonant converters are different, the integrated charger is not able to provide the simultaneous operation.

From the brief overview mentioned above, it can be seen that the previously existing integrated chargers have at least one of the following drawbacks.

1) The OBC and the APM cannot operate simultaneously or an extra component is required for simultaneous operation.
2) Extra relays are required for mode change.
3) Galvanic isolation between HV batteries and grid is not provided.
4) Overall efficiency is decreased by extra components or multistage power process of APM.
5) Complex design and large volume of transformer is required due to multiwinding transformer.

This article proposes an APM integrated OBC eliminating the above-mentioned problems. The proposed integration concept, the proposed dc-link control method, and the operation principles are presented in Section II. Design methods and comparative studies are discussed in Sections III and IV, respectively. In Section V, the experiment result from the laboratory prototype of the proposed integrated charger is provided to verify the theoretical analysis. Finally, Section VI concludes the article.

II. Proposed Integrated Charger

A. Concept of the Proposed Integration

The schematic diagram of the separated OBC and APM that are separately connected to the HV battery is shown in Fig. 2(a). The OBC has two-stage structure that consists of a front-end ac–dc converter for power factor correction and an isolated dc–dc converter for HV battery voltage/current regulation and galvanic isolation. The APM has single-stage structure for LV battery voltage/current regulation and galvanic isolation.

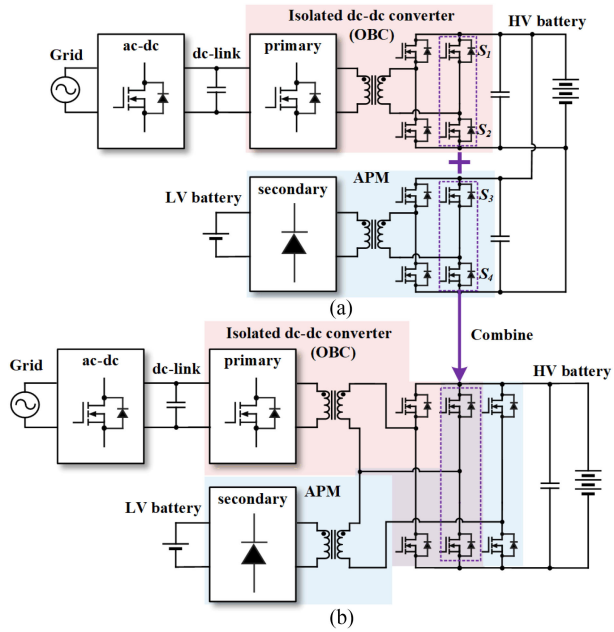

Fig. 2. Schematic diagram of the (a) separated OBC and APM and the (b) proposed integrated charger.

The schematic diagram of the proposed integrated charger is shown in Fig. 2(b). The concept of the proposed integration is combining a secondary leg of the OBC (S_1 and S_2) and a primary leg of the APM (S_3 and S_4) into a common leg which performs both independent and simultaneous operations of the OBC and the APM, resulting in reduced number of switches. The proposed integration makes the OBC and the APM share HV-side components such as filter capacitors, EMI filters, and cables. The proposed integration concept can be applied to the OBC with the resonant-based converter or the dual-active-bridge (DAB)-based converter. The resonant converters are preferable due to inherent characteristics of entire range ZVS operation and small turn-OFF current.

B. Adaptive DC-Link Control Scheme for Use of LLC Converter Under Wide Range Bidirectional Operation

In general, two types of control schemes can be considered for the two-stage OBC with the resonant converter—constant dc-link scheme [3] or variable dc-link scheme [4]–[6]. In the variable dc-link control scheme, the wide HV battery voltage is regulated by the ac–dc converter while the resonant converter compensates only for the second-harmonic ripple of the dc-link. This allows the converter to operate at near unity gain with narrow frequency control. As a result, the overall efficiency of the OBC is increased compared to the constant dc-link scheme while the cost and volume are increased by high voltage rating (more than 700 V) components.

Although the CLLLC resonant converter is popular for bidirectional operation due to symmetrical gain in both power flow directions, the five resonant components increase the volume, cost, and the complexity of design. The LLC resonant converter has less resonant component count than the CLLLC resonant

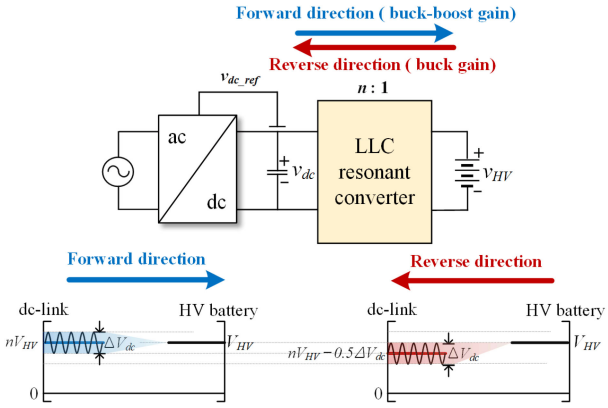

Fig. 3. Proposed adaptive dc-link control scheme for use of the LLC resonant converter under wide range bidirectional operation.

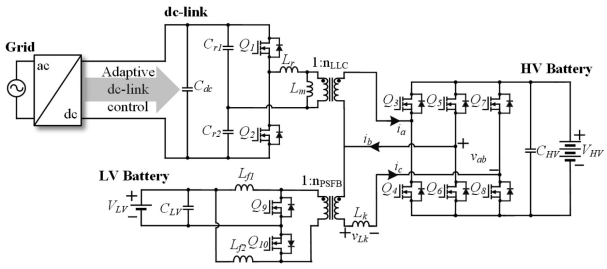

Fig. 4. Schematic circuit of the proposed integrated charger.

converter. However, different voltage gain in each direction due to asymmetrical resonant tank makes it difficult to be used in bidirectional power flow.

This article proposes an adaptive dc-link control scheme for use of the LLC resonant converter under wide range bidirectional operation. Fig. 3 shows the proposed adaptive dc- link control. The ac–dc converter adjusts the dc-link voltage to different values according to the power flow as in the following:

$$\begin{cases} v_{\mathrm{dc-ref}} = nV_{\mathrm{HV}}, \text{ Forward direction} \\ v_{\mathrm{dc-ref}} = nV_{\mathrm{HV}}\Delta V_{\mathrm{dc}}, \text{ Reverse direction} \end{cases}. \quad (1)$$

In forward direction, the dc-link voltage is set to nV_{HV} that provides unity gain to the LLC resonant converter. Then, the LLC resonant converter compensates for the second-harmonic ripple using small variation of buck–boost gain. In reverse direction, the dc-link voltage is slightly reduced such that the peak of the dc-link voltage does not exceed the unity gain nV_{HV} while compensating for the second-harmonic ripple using small variation of buck gain. This adaptive dc-link control makes the LLC resonant converter viable for wide range bidirectional operation instead of the CLLLC resonant converter.

C. Operating Principles of the Proposed Integrated Charger

Fig 4 shows the schematic circuit of the proposed integrated charger that employs a half-bridge LLC resonant converter with the adaptive dc-link control and a phase-shift full-bridge (PSFB) converter with current doubler (CD) rectifier. The PSFB

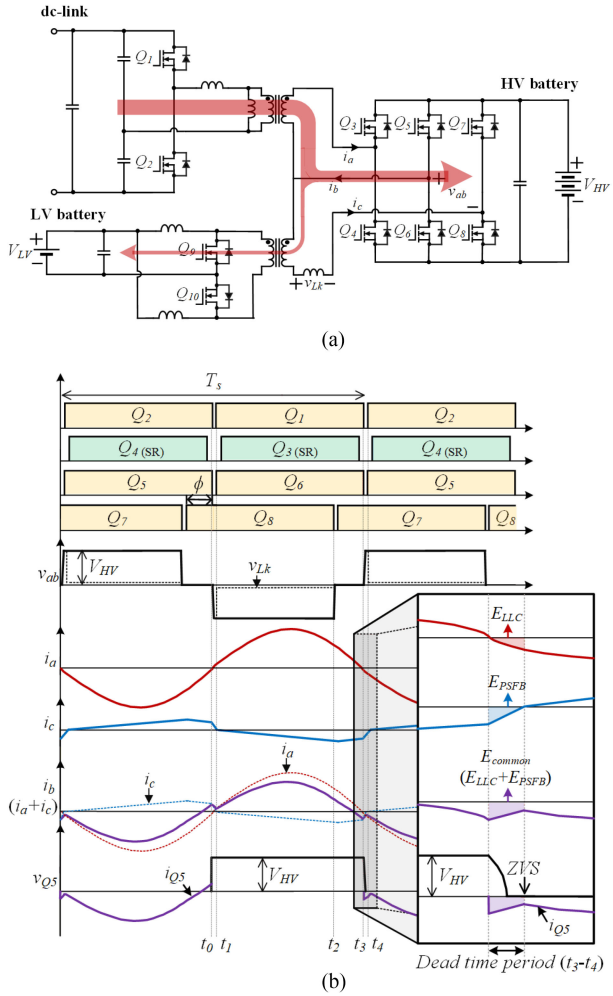

Fig. 5. Operation principle during the simultaneous charging mode. (a) Power flow. (b) Key waveform.

converter is mainly employed for the APM due to simple structure and wide range operation, and the CD rectifier has lower transformer turn ratio and reduced secondary winding current compared to the center-tap rectifier. In addition, synchronous rectification (SR) in LV side is applied to increase the efficiency.

When the vehicle is connected to the grid for charging or discharging the HV battery, the OBC operates mainly under full-load condition and APM operate below the 400-W condition. When the vehicle is driven, only the APM operates to charge the LV battery, mainly under light load condition. The proposed integrated charger has three operation modes—simultaneous charging mode, V2G mode, and the APM standalone operation. Detailed operating principles for the three modes are provided.

1) Simultaneous Charging Mode: In the separated OBC and APM shown in Fig. 2(a), the LV battery is charged from the HV battery while the HV battery is charged from the grid. However, in the proposed integrated charger, as shown in Fig. 5(a), the LV battery is *directly* charged from the grid while the LLC resonant converter charges the HV battery, resulting in high overall efficiency, which can be explained by current cancellation. The key waveform of the simultaneous charging mode is shown

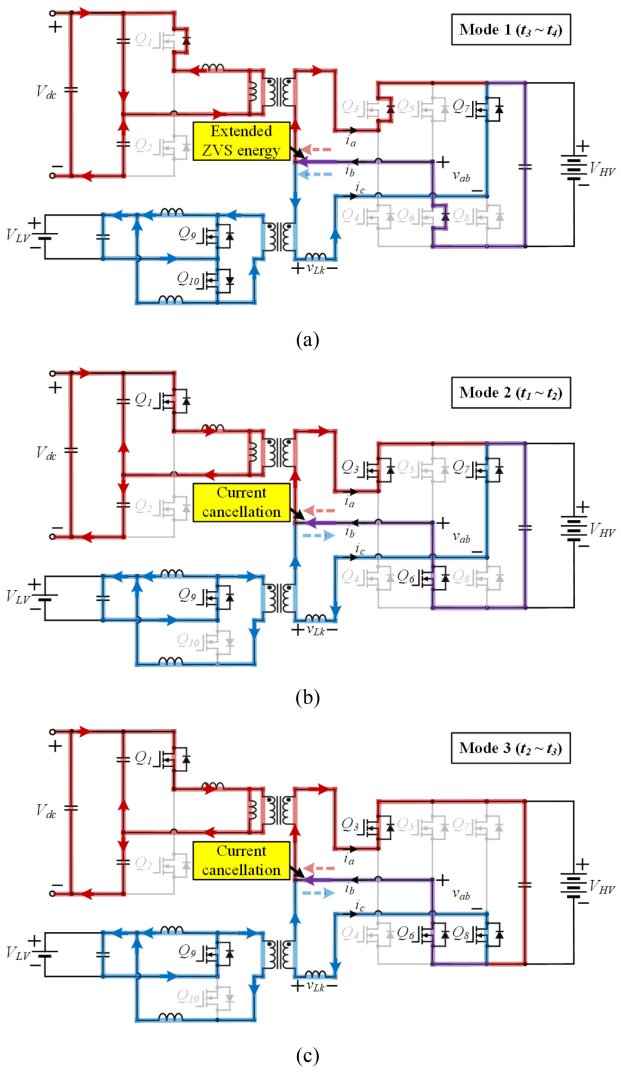

Fig. 6. Operation stages of the proposed integrated charger during the simultaneous charging mode. (a) Mode1 (t_0–t_1). (b) Mode 2 (t_1–t_2). (c) Mode 3 (t_2–t_3).

in Fig. 5(b). The LLC resonant converter operates at nearly unity gain while the PSFB converter operates with phase-shift duty (Φ) between the lagging leg (Q_5, Q_6) and the leading leg (Q_7, Q_8). Q_3 and Q_4 are operated as synchronous rectifier for forward direction of the LLC resonant converter. i_a and i_c are secondary current of the LLC resonant converter and primary current of the PSFB converter, respectively, and i_b is the sum of i_a and i_c as follows:

$$i_b(t) = i_a(t) + i_c(t). \tag{2}$$

Fig. 6 shows the operation stages of the proposed integrated charger during the simultaneous charging mode. Three operation stages are presented in order to show the main advantages of the proposed integrated charger during the simultaneous charging mode clearly.

1) *Mode 1* [t_0–t_1]: When Q_2, Q_4, and Q_5 are turned OFF, the output capacitors of Q_1–Q_6 are charged or discharged. After that, the body diodes of Q_1, Q_3, and Q_6 are conducted for ZVS operation. And the LV-side switches Q_9 and Q_{10} start commutating together. Since the voltage across the leakage inductor is $-V_{\rm HV}$, i_c is decreased sharply and no energy is transferred from HV battery to LV battery. And ZVS current for lagging leg switch Q_6 is increased due to the same polarity of i_a and i_c.
2) *Mode 2* [t_1–t_2]: The primary current of the PSFB converter i_c is reflected by filter inductor current on LV side and energy from the HV battery is transferred to the LV battery. The magnitude of i_b is decreased by the opposite polarity of i_a and i_c.
3) *Mode 3* [t_2–t_3] : During this period, no energy is transferred to the LV battery from the HV battery due to zero voltages of $v_{\rm ab}$ and the magnitude of i_b is still decreased by the opposite direction of i_a and i_c.

Assuming that the switching frequency is the same as the resonant frequency, the secondary current of LLC resonant converter i_a can be expressed by the following equations during the half-switching period [t_0–t_3]:

$$i_a(t) = \frac{\pi}{2V_{\rm HV}} p_{\rm charging} \mathrm{Sin}(2\pi f_r(t-t_0)), t_0 \le t \le t_3. \tag{3}$$

And the primary current of the PSFB converter i_c in continuous conduction mode operation is also expressed by the following equations during the half-switching period [t_0–t_3]:

$$\begin{cases} i_c(t) = i_c(t_0) - \frac{V_{\rm HV}}{n_{\rm PsFB} L_k}(t-t_0), & t_0 \le t \le t_2 \\ i_c(t) = i_c(t_1) - \frac{V_{\rm HV} - n_{\rm PsFB} V_{LV}}{n^2_{\rm PsFB} L_{f1}}(t-t_1), & t_1 \le t \le t_2 \\ i_c(t) = -\frac{V_{\rm LV}}{n_{\rm PsFB} L_{f1}}\left(t - \frac{T_s + t_1 + t_2}{2}\right) - \frac{P_{\rm APM}}{2 n_{\rm PsFB} L_{\rm LV}}, t_2 \le t \le t_3. \end{cases} \tag{4}$$

Operating the common leg as the lagging leg helps the magnitude of the common leg current i_b to be reduced by current cancellation effect. Except duty loss period [t_0–t_1], polarities of the secondary current of LLC resonant converter i_a and the primary current of PSFB converter i_c are opposite. Since duty loss period is very short in light load condition of the APM, this period can be neglected. That is, the common leg current i_b is decreased by i_c compared to i_a, resulting in decreased conduction loss. The rms value of each leg current of the proposed integrated charger can be calculated from (2)–(4) and the conduction losses are compared to the separated OBC and APM according to HV charging power, as shown in Fig. 7. Conduction loss of four switches (S_1–S_4) of the separated charger in Fig. 2(a) is higher than that of the common leg switches of the proposed integrated charger under entire load range. It is noted that the proposed integrated charger not only reduces the number of switches but also has lower conduction loss due to the current cancellation effect compared to the separated OBC and APM.

In the conventional PSFB converter, ZVS energy of the lagging leg switch may not be sufficient to achieve ZVS operation under light load condition. ZVS operation even under light load condition is important since the APM usually operates under 400 W in the simultaneous operation. The proposed integrated charger can extend the ZVS range of the lagging leg by operating the common leg as the lagging leg of the PSFB converter. That is, as shown in Fig. 5(b), the ZVS energy of the lagging leg

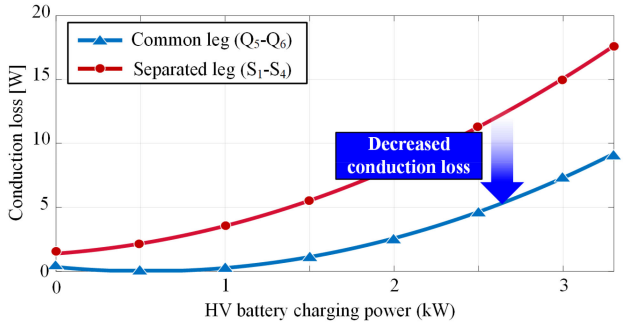

Fig. 7. Conduction loss comparison of common leg switches and separated leg switches according to HV charging power (V_{HV}= 330 V, V_{LV}=13 V, P_{APM} = 0.4 kW).

switches of the proposed integrated charger E_{common} during the dead-time period [t_3–t_4] is increased by the ZVS energy of the LLC resonant converter E_{LLC}.

Three HV-side legs operate as two independent full-bridges for OBC and APM; full bridge switches for OBC are Q_3–Q_6 and full-bridge switches for APM are Q_5–Q_8. That is, two batteries are independently regulated by different control variables. And, i_a and i_c are determined by the HV battery current and LV battery current, respectively, which means that sudden load change on one terminal does not affect the other terminal.

2) V2G Mode: In the V2G mode, the LLC resonant converter discharges the HV battery to the grid while the PSFB converter charges the LV battery, as shown in Fig. 8(a). The key waveform of the V2G mode is shown in Fig. 8(b). The LLC resonant converter operates with reverse direction with buck gain. The operating switching frequency of the LLC resonant converter is slightly higher than the resonant frequency due to ZVS operation. The operation of the PSFB converter of the V2G mode is the same as that of the simultaneous charging mode. And Q_1 and Q_2 are operated as synchronous rectifiers for reverse power flow of the LLC resonant converter. Although i_b is increased due to the same polarity of i_a and i_c, ZVS energy of the common leg is also increased by reverse operation of the LLC resonant converter, as shown in Fig. 8(b).

3) APM Standalone Mode: The proposed integrated charger has two switching methods according to load condition for entire range ZVS operation of the lagging leg switches in the APM standalone mode. Under medium to heavy load condition, the PSFB converter normally operates with full-bridge switches (Q_5–Q_8), as shown in Fig. 9, achieving ZVS operation of the lagging leg switches due to sufficient ZVS energy. ZVS energy of the lagging (common) leg switch Q_5 can be expressed by

$$E_{\mathrm{common}} = E_{\mathrm{PSFB}} = \frac{1}{2} L_k (i_c^2(t_3) - i_c^2(t_4)). \tag{5}$$

However, since the ZVS energy of the lagging leg switches may not be sufficient to achieve ZVS operation under light load condition, a method of increasing ZVS energy of the lagging leg switches utilizing LLC converter switches Q_3 and Q_4 is proposed, as shown in Fig. 10(a). The LLC converter switches Q_3 and Q_4 operate in a diagonal manner with common leg

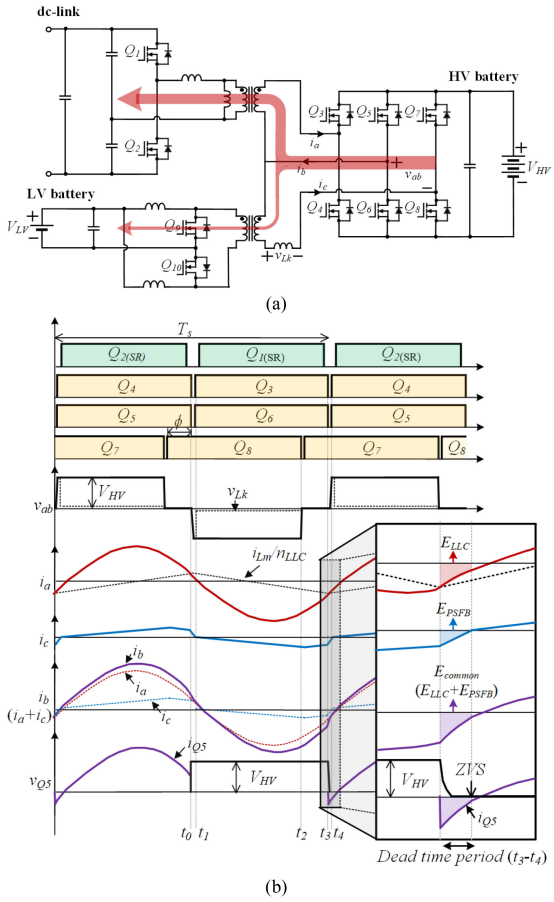

Fig. 8. Operation principle during the V2G mode. (a) Power flow. (b) Key waveform.

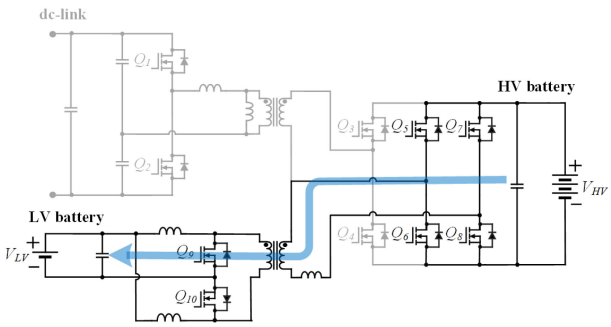

Fig. 9. Switch operation of the APM standalone mode under medium-heavy load condition.

switches under light load condition, as shown in Fig. 10(b), and ZVS current of the lagging leg switches is increased by the magnetizing current of the LLC resonant converter, leading to increased ZVS energy. The magnitude of the increased ZVS current by the magnetizing current is given by

$$i_a(t) = \frac{V_{\mathrm{HV}} T_s}{4 L_m n_{\mathrm{LLC}}^2} - \frac{V_{\mathrm{HV}}(t - t_0)}{L_m n_{\mathrm{LLC}}^2}, \; t_0 \le t \le t_3. \tag{6}$$

Fig. 11 shows a comparison of ZVS energy of the lagging leg switch of the proposed integrated charger with that of the

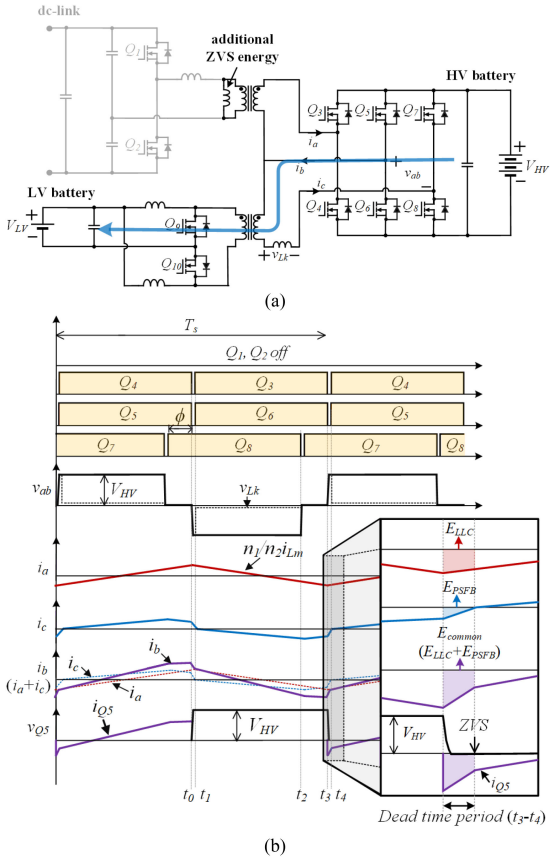

Fig. 10. Operation principle during the APM standalone mode under light load condition. (a) Switch operation. (b) Key waveform.

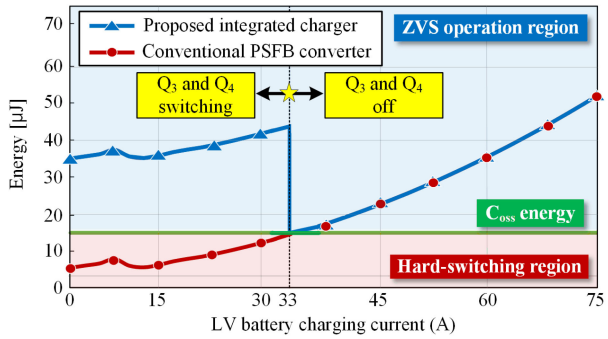

Fig. 11. Operating switching frequency range of the proposed integrated charger for the adaptive dc-link control ($V_{\mathrm{HV}} = 240\,\mathrm{V}$, P_{charging} and $P_{\mathrm{V2G}} = 2.4\,\mathrm{kW}$).

separated PSFB converter. When ZVS energy is higher than output capacitor energy (E_{oss}), ZVS operation is achieved. E_{oss} is given by

$$E_{\mathrm{oss}} = \frac{1}{2} C_{\mathrm{oss}} V_{\mathrm{HV}}^2. \tag{7}$$

When the LV battery charging current becomes lower than 33 A, Q_3 and Q_4 of the proposed integrated charger start operating to achieve ZVS turn-ON of the common leg switches, whereas lagging leg switches of the separated PSFB converter

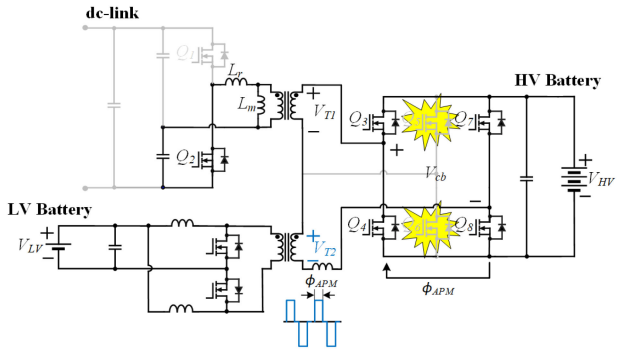

Fig. 12. APM standalone mode in case of the open-circuit fault of the common leg.

are hard switched. Therefore, the proposed integrated charger achieves entire voltage and load range ZVS operation.

Operating Q_3 and Q_4 at the light load condition does not affect the regulation of the LV battery since v_{ab} is dependent only on the PSFB converter switches (Q_5–Q_8). Therefore, there is no transient issue associated with the operation of Q_3 and Q_4 in the proposed APM standalone mode, and the performance of the APM is the same as that of the separated one.

Further, since the current rating of the common leg switch (Q_5 and Q_6) is determined by the OBC operation, use of the common leg switches for the APM standalone operation results in reduced conduction loss due to smaller $R_{\mathrm{ds(on)}}$ of the common leg switches compared to that of Q_7 and Q_8.

In the integrated charger which commonly uses the switch leg, failure of the common leg makes the whole APM be disabled. It cannot be justified as the main vital controls of the EVs are on the LV bus. In case of the open-circuit fault of the common switch leg, the proposed integrated charger provides the fault-mitigating operation mode. Fig. 12 shows the APM standalone mode in case of the open-circuit fault of the common leg. One of Q_1 or Q_2 of the dc-link side is turned ON, and then, the primary winding of the LLC transformer is short circuited, which makes switches Q_3–Q_4 and Q_7–Q_8 play the role of the primary bridge of the PSFB converter. The magnetizing inductance and resonant inductance of the LLC resonant converter are equivalent with additional series inductor of the PSFB converter. The equivalent series inductance L_{eq} value is expressed as

$$L_{\mathrm{eq}} = L_k + \frac{n_{\mathrm{LLC}} L_r L_m}{L_r + L_m}. \tag{8}$$

This large series inductance value makes the APM power derated due to large duty loss period, while increasing the ZVS energy of the lagging leg switches.

III. Design Procedure

A. Design of the LLC Resonant Converter for Adaptive DC-Link Control

Since the switching frequency of the PSFB converter follows that of the LLC resonant converter during the simultaneous operation, narrow operating frequency range of the LLC resonant

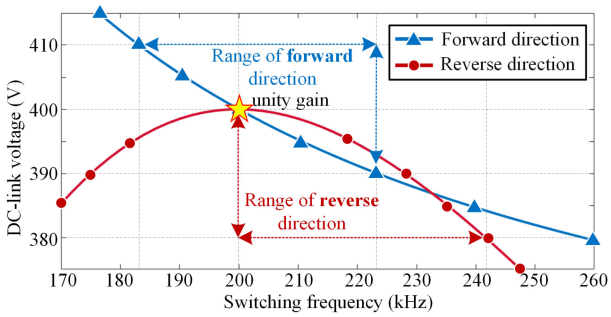

Fig. 13. Operating switching frequency range of the proposed integrated charger for the adaptive dc-link control ($V_{\mathrm{HV}} = 240\,\mathrm{V}$, P_{charging} and $P_{\mathrm{V2G}} = 2.4\,\mathrm{kW}$).

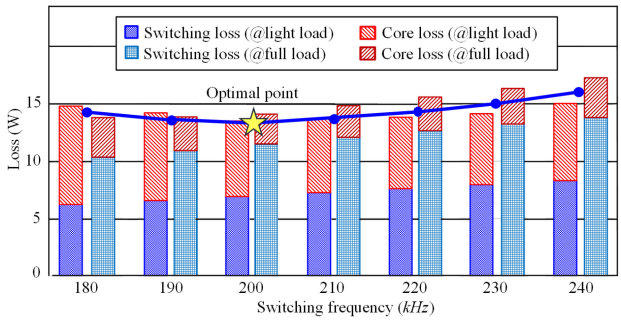

Fig. 14. Selection of the switching frequency of the PSFB converter for APM standalone mode.

converter is preferred. DC-link voltage range is considered to be 380–700 V when $V_{\mathrm{HV}} = 240$–$420\,\mathrm{V}$ (see Table III). DC-link capacitance is designed to be $950\,\mu\mathrm{F}$ considering the lifetime of electrolytic capacitor, which results in the maximum voltage ripple of dc-link of 20 V at $V_{\mathrm{HV}} = 240\,\mathrm{V}$ by

$$\Delta V_{\mathrm{dc}} = \frac{P_{\mathrm{OBC}}}{2\pi f_{\mathrm{grid}} V_{\mathrm{dc}} C_{\mathrm{dc}}}. \tag{9}$$

Fig. 13 shows the operating switching frequency range of the proposed integrated charger for the adaptive dc-link control. When $V_{\mathrm{HV}} = 240\,\mathrm{V}$, the dc-link voltage range is 390–410 V for forward power flow and 380–400 V for reverse power flow, respectively. Considering the required voltage gain range for both forward and reverse power flow and 20% switching frequency variation of 184–243 kHz, the resonant component values can be obtained as $L_m = 101.3\,\mu\mathrm{H}$, $L_r = 13.6\,\mu\mathrm{H}$, and $C_r = 46.5\,\mathrm{nF}$ (see Table III). The magnetizing inductance value L_m is sufficient to charge and discharge the C_{oss} of the switches leg of the LLC resonant converter during the dead-time period.

B. Optimal Operation of the PSFB Converter in the APM Standalone Mode

In the APM standalone mode, the PSFB converter operates at a fixed switching frequency between 184 and 243 kHz. An optimal switching frequency is selected, as shown in Fig. 14, considering the core loss and switching loss according to switching frequencies. At the light load condition (200 W), additional core loss of the LLC resonant converter is generated by operating

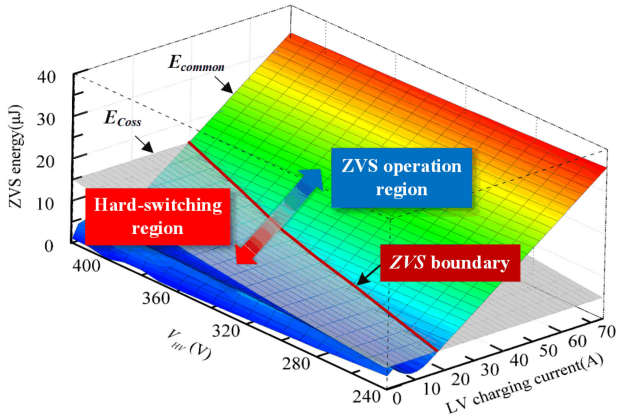

Fig. 15. ZVS boundary of the separated PSFB converter.

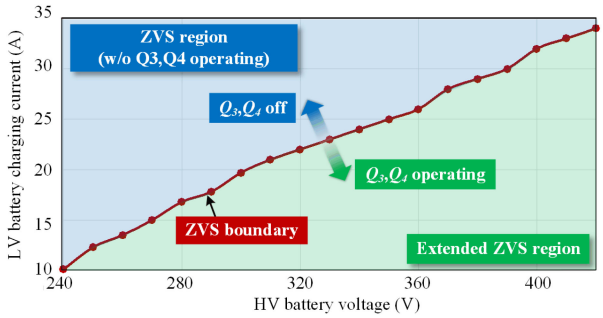

Fig. 16. Boundary of the operating the Q_3 and Q_4.

Q_3 and Q_4. The core loss at switching frequency of 180 kHz is largest due increased volt-sec of the two transformers. On the other hand, at the full load condition (1 kW), the switching loss is highest at switching frequency of 240 kHz. Therefore, switching frequency of 200 kHz is selected for the APM standalone operation considering both full load condition and light load condition.

Since operating Q_3 and Q_4 for extending the ZVS operation range of the lagging leg switches generates additional core loss and switching loss, it should be carefully determined considering the LV charging current and HV battery voltage condition. Fig 15 shows the ZVS boundary of the lagging leg switches without operating Q_3 and Q_4. ZVS energy of the lagging (common) leg switches E_{common} is proportional to LV charging current, and E_{oss} is proportional to HV battery voltage. The ZVS boundary can be obtained with $E_{\mathrm{common}} = E_{\mathrm{oss}}$. Fig. 16 shows the boundary of the operating Q_3 and Q_4 considering ZVS boundary of lagging leg switches. Q_3 and Q_4 operate when ZVS energy of the lagging leg switches is lower than E_{oss}. Therefore, entire range ZVS operation of the lagging leg switches can be achieved by operating Q_3 and Q_4 based on the operation boundary that is the same as the ZVS boundary in Fig. 15.

IV. Comparative Studies

In order to show the effectiveness of the proposed integrated charger, the proposed integrated charger is compared with the separated OBC and APM in Fig. 2(a) in terms of cost, volume,

TABLE I
COMPARISON WITH THE EXISTING INTEGRATED CHARGER

Topology (OBC, APM)	Proposed	[24]	[25]	[31]	[32]
	LLC, PSFB	DAB, DAB+buck	buck-boost , LLC	PSFB, PSFB	CLLC, LLC
Galvanic isolation	O	X	X	O	O
Key integration components	switches	switches	switches	transformer	transformer
Number of relay for integration	0	1	1	1	1
Simultaneous operation	O	X	O (with extra circuit)	O (with extra circuit)	X
Entire load ZVS range	O	X	X	X	O

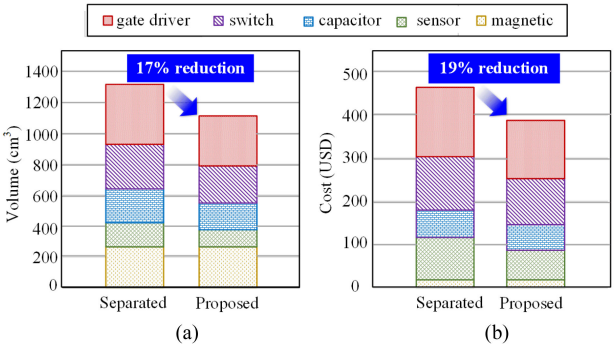

Fig. 17. (a) Volume and (b) cost comparison of the proposed integrated charger and the separated charger.

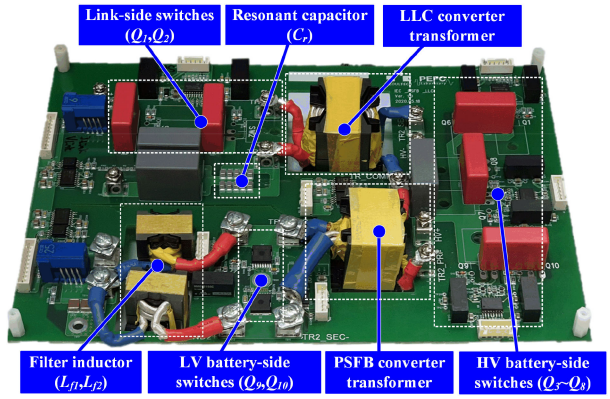

Fig. 18. Prototype of the proposed integrated charger.

and efficiency. Fig. 17(a) and (b) shows the volume and cost comparisons. Overall volume and cost of the proposed integrated charger are decreased by 17% and 19%, respectively, due to reduced switches count and shared input filter. The efficiency of the proposed integrated charger is shown to be higher at both simultaneous mode and APM standalone mode (see Figs. 21 and 25).

Table I shows the comparison of the proposed integrated charger to existing integrated chargers [24], [25], [31], [32]. The proposed integrated charger provides low profile due to the use of two small transformers compared to the transformer integration method using a three-winding transformer [31], [32]. The proposed integrated charger does not necessitate extra relay for integration and additional circuit for simultaneous operation unlikely the existing integrated chargers. In addition, the proposed integrated charger achieves the entire ZVS range of all switches of the PSFB converter in both simultaneous charging/V2G mode and the APM standalone operation modes. If the common leg fails, the whole APM is disabled in the existing integrated charger. However, the proposed integrated charger can deliver the partial power to the LV battery, while achieving ZVS operation of the lagging leg switches. Therefore, the proposed integrated charger clearly stands out from not only the separated OBC and APM but also the existing integrated chargers.

V. EXPERIMENT RESULT

In order to verify the performance of the proposed integrated charger, a laboratory prototype integrating 3.7-kW LLC resonant converter and 1-kW PSFB converter is built on a PCB board, as illustrated in Fig 18. The LLC resonant converter and the PSFB converter share the heatsink, HV battery-side filters, and sensors. The key parameters and system specifications of the proposed integrated charger are summarized in Tables II and III, respectively. The dc-link side and HV-side switches were implemented using SiC devices (Q_1, Q_2: E3M0065090D from Cree, Q_3–Q_6: SCT3080AL from Rohm, Q_7, Q_8: SCT3120AL from Rohm) and LV-side switches were implemented using Si device (Q_9, Q_{10}: IAUT300N10S5N015 from Infineon). The transformer and filter inductor were implemented with PL15 ferrite cores from Samwha electronics (PQ40/40 for LLC resonant converter, PQ35/35 for the PSFB converter, and PQ26/25 for the PSFB filter inductors L_{f1} and L_{f2}). The control algorithm is implemented in a floating-point DSP platform TMS320F38377D. And, the digital power meter YOKOGAWA WT3000 is used to measure the efficiency.

TABLE II
KEY PARAMETERS OF THE PROPOSED INTEGRATED CHARGER

Parameters		Symbol	Values
LLC resonant converter	Dc-link side switches	Q_1, Q_2	900V, 65mΩ
	HV-side switches	Q_3, Q_4	650V, 80mΩ
	Magnetizing inductance	L_m	101.3μH
	Resonant inductance	L_r	13.6μH
	Resonant capacitance	C_r	46.5nF
	Resonant frequency	f_r	200kHz
	Transformer turn ratio	n_{LLC}	1.2
	Dc-link side filter capacitance	C_{dc}	950μF
	HV battery-side filter capacitance	C_{HV}	20μF
PSFB converter	HV-side switches	Q_7, Q_8	650V, 120mΩ
	LV-side switches	Q_9, Q_{10}	100V, 1.5mΩ
	Leakage inductance	L_k	3.8μH
	Filter inductance	L_{f1}, L_{f2}	2.7μH
	Transformer turn ratio	n_{PSFB}	6.5
	LV battery-side filter capacitance	C_{lv}	66μF
Common leg switches		Q_5, Q_6	650V, 80mΩ
Switching frequency		f_{sw}	184kHz~243kHz

TABLE III
SYSTEM SPECIFICATIONS OF THE PROPOSED INTEGRATED CHARGER
(V_{HV}:240–420 V, V_{LV}:11–14 V)

Operation condition	Parameter	Value (unit)
Simultaneous Mode	HV battery charging power ($P_{charging}$) /discharging power (P_{V2G})	3.3kW
	LV battery charging power (P_{APM})	0.4kW
	Maximum HV battery current	10A
	Maximum LV battery current	30A
	DC link voltage (V_{dc})	380V-700V
APM Standalone Mode	LV battery charging power (P_{APM})	1kW
	Maximum LV battery current	74A

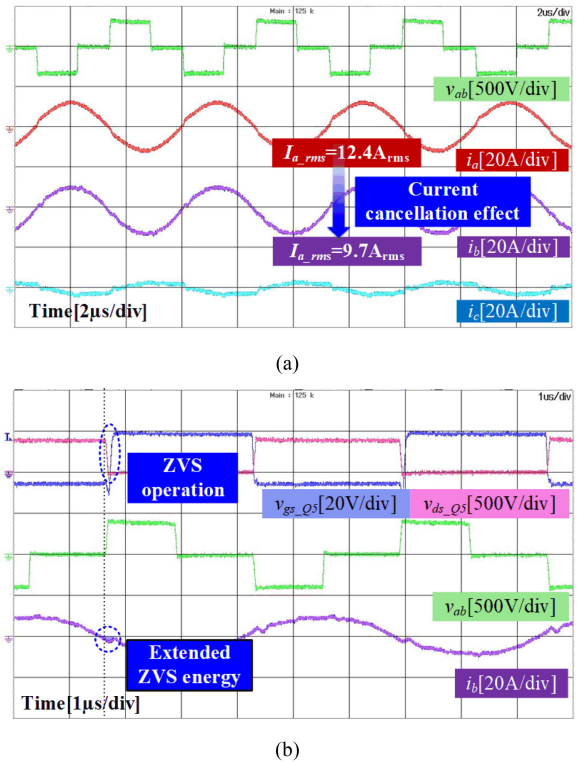

Fig. 19. Experimental waveforms during the simultaneous charging mode ($P_{charging}$ = 3.3 kW, P_{APM} = 0.4 kW, and V_{LV} = 13 V). (a) Each leg current at V_{HV} = 330 V. (b) ZVS operation of the lagging leg switch Q_5 at V_{HV} = 420 V.

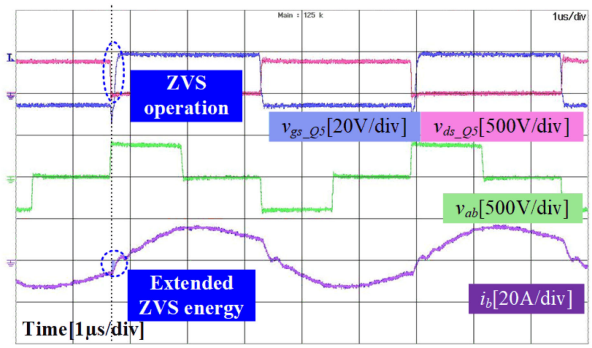

Fig. 20. ZVS operation of the lagging leg switch Q_5 at V_{HV} = 420 V during the V2G mode (P_{V2G} = 3.3 kW, P_{APM} = 0.4 kW, and V_{LV} = 13 V) .

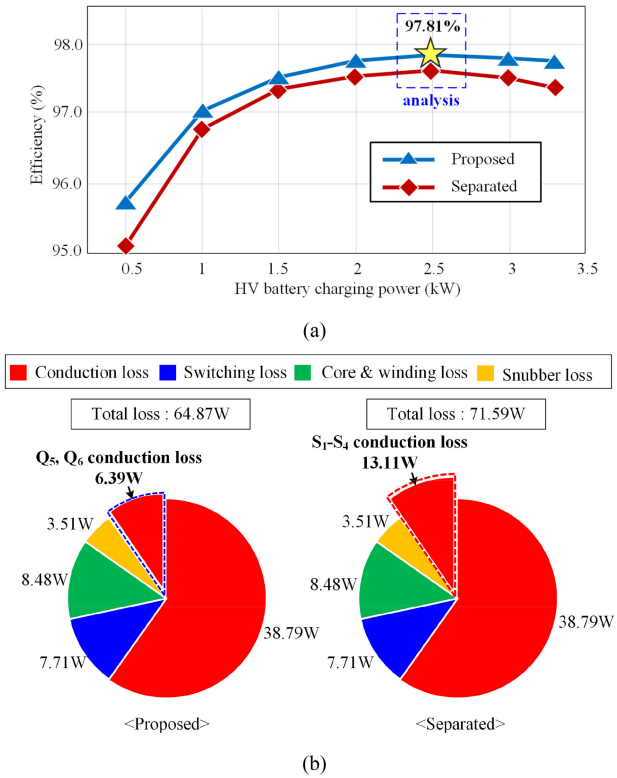

Fig. 21. (a) Measured efficiency when V_{HV}=330 V, V_{LV}=13 V, and P_{APM}= 0.4 kW. (b) Loss analysis when $P_{charging}$=2.5 kW during the simultaneous mode.

Fig. 19 shows the key waveform of the proposed integrated charger in the simultaneous charging mode. The common leg current i_b is the sum of LLC resonant converter secondary current i_a and the PSFB converter primary current i_c, as shown in Fig. 19(a). As a result, rms value of the common leg current i_b is reduced by 2.7 A compared to i_a by the current cancellation effect. Fig. 19(b) shows ZVS operation of the common leg switch Q_5 when the PSFB converter operates under light load condition. ZVS energy of the common leg switch Q_5 is extended by secondary current of the LLC resonant converter. Fig. 20 shows the key waveform of the proposed integrated charger in the V2G mode. The ZVS operation of the lagging leg switch Q_5 is also achieved by extended ZVS energy.

Efficiencies of each simultaneous mode are considered for only dc–dc parts except ac–dc converter. Fig. 21(a) shows the measured efficiency in the simultaneous charging operation when V_{HV} = 330 V, V_{LV} = 13 V, and P_{APM} = 0.4 kW. The maximum efficiency is 97.81% when $P_{charging}$ is 2.5 kW, and overall efficiency in simultaneous charging mode is around 0.5% higher than the separated charger by current cancellation effect. The loss analysis of the proposed integrated charger and separated charger in the simultaneous charging mode when $P_{charging}$ = 2.5 kW is shown in Fig. 21(b). By current cancellation effect, conduction loss of common leg switches (Q_5 and Q_6) are almost

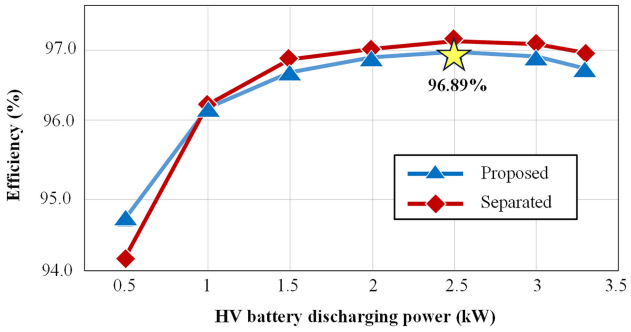

Fig. 22. Measured efficiency during the V2G mode when V_{HV}=330 V, V_{LV}= 13 V, and P_{APM}=0.2 kW.

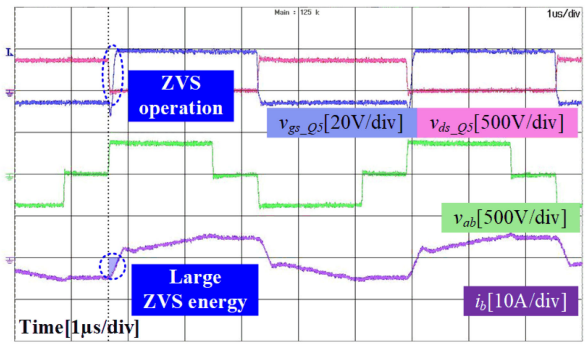

Fig. 23. ZVS operation of the lagging leg switch Q_5 at V_{HV} = 420 V during the APM standalone mode when V_{HV}=420 V, V_{LV} = 13 V, and P_{APM}=1 kW.

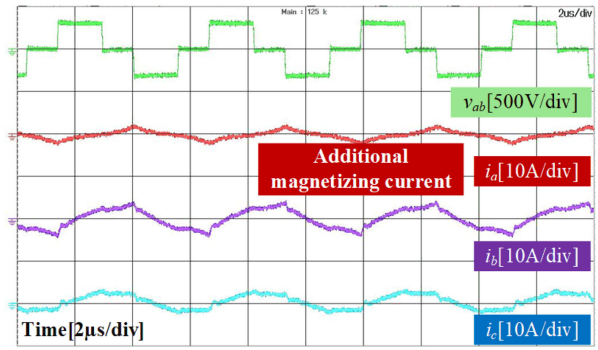

(a)

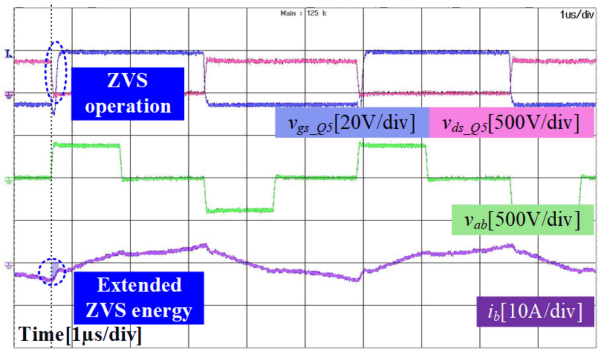

(b)

Fig. 24. Experimental waveforms during the APM standalone mode (P_{APM} = 0.2 kW and V_{LV} = 13 V). (a) Each leg current at V_{HV} = 330 V. (b) ZVS operation of the lagging leg switch Q_5 at V_{HV} = 420 V.

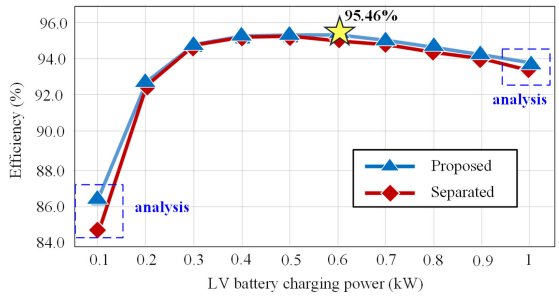

(a)

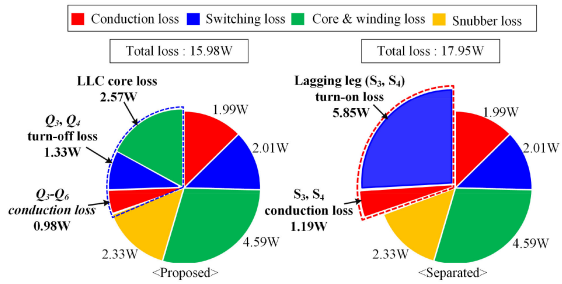

(b)

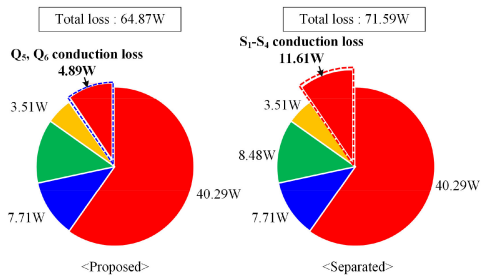

(c)

Fig. 25. (a) Measured efficiency when *V*HV=240 V and *V*LV=13 V, and loss analysis when (b) *P*APM=0.1 kW and (c) *P*APM=1 kW during the APM standalone mode.

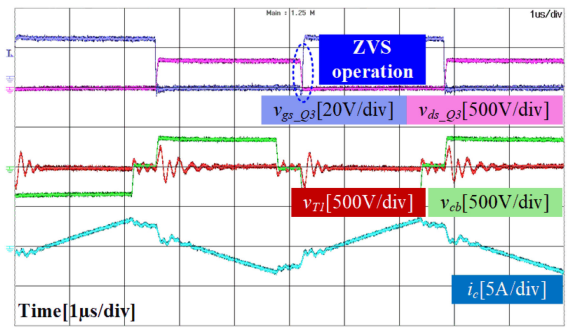

Fig. 26. Experimental waveforms of the APM standalone mode in case of open-circuit fault of the common leg switches (P_{APM} = 0.2 kW, V_{HV}=330 V and V_{LV} = 15 V).

half of the separated leg switches (S_1–S_4), while the rest of losses are the same. Fig. 22 shows the efficiency of the V2G mode when V_{HV} = 330 V, V_{LV} = 13 V, and P_{APM} = 200 W, and the maximum efficiency is 96.89% when P_{V2G} = 2.5 kW. Since the rms value of the common leg switches is increased by the same direction as i_a and i_c, the overall efficiency is lower than the separated charger at medium to heavy load condition. However,

the light load efficiency is higher than the separated charger due to ZVS operation of the lagging leg switches.

Fig. 23 shows the ZVS operation of the lagging leg switch Q_5 in the APM standalone mode under full load condition. In the full load condition, the ZVS energy of the lagging leg switches is sufficient to achieve ZVS operation. Under the light load condition, the magnetizing current of the LLC resonant converter transformer is generated by operating Q_3 and Q_4, as shown Fig. 24(a), which leads to extended ZVS energy of the lagging leg switch Q_5, as shown Fig. 24(b), resulting in ZVS operation of Q_5.

Fig. 25(a) shows the efficiency of the APM standalone mode when $V_{\rm HV} = 240\,{\rm V}$ and $V_{\rm LV} = 13\,{\rm V}$. The peak efficiency is 95.46% when $P_{\rm APM} = 0.6\,{\rm kW}$, and overall efficiency is higher than the separated charger. Fig. 25(b) and (c) shows the loss analysis of the proposed integrated charger and separated charger under $P_{\rm APM} = 0.1\,{\rm kW}$ and $P_{\rm APM} = 1\,{\rm kW}$, respectively. When $P_{\rm APM} = 0.1\,{\rm kW}$, the proposed integrated charger achieves ZVS operation of the lagging leg switches by operating Q_3 and Q_4. However, the lagging leg switches of the separated charger are hard-switched. Due to turn-ON loss of the lagging leg switches, the loss of the proposed integrated charger is lower than the separated charger. When $P_{\rm APM} = 1\,{\rm kW}$, switching methods of the proposed integrated charger and separated charger are the same. But, $R_{\rm ds(on)}$ value of the common leg switches ($80\,{\rm m}\Omega$) is smaller than that of the separated leg switches ($120\,{\rm m}\Omega$). Therefore, the conduction loss of the proposed integrated charger is 66% smaller than the separated charger.

Fig. 26 shows the APM standalone mode in case of open-circuit fault of the common leg in Fig. 12 when $P_{\rm APM} = 200\,{\rm W}$, $V_{\rm HV} = 330\,{\rm V}$, and $V_{\rm LV} = 13\,{\rm V}$. Although the power of the APM is limited due to increasing duty-loss period, ZVS operation under light load condition is ensured by increased ZVS energy.

VI. Conclusion

This article proposes an APM integrated OBC that makes simultaneous operation possible without employing relays and extra circuits. In the simultaneous mode, the conduction loss is decreased by the current cancellation effect and entire ZVS operation is achieved by extended ZVS energy of the common leg switches, resulting in increased, in particular, light load efficiency. In the APM standalone mode, operating the switch leg of the LLC resonant converter according to the optimized ZVS boundary ensures entire ZVS operation. From the prototype integrating a 3.7-kW LLC resonant converter with a 1-kW PSFB converter, it is shown that the overall efficiency is increased by 0.5% compared to the separated charger, and maximum efficiency reaches up to 97.61% in the simultaneous mode. In the APM standalone operation, the light load efficiency is increased up to 2% compared to the separated APM by entire load ZVS operation and the peak efficiency reaches up to 95.46%. It should be noted that in addition to the efficiency improvement, the volume and cost are also reduced by 17% and 19%, respectively, compared with the separated OBC and APM, since the proposed integration does not require extra components, and the APM components, including two primary switches, gate drivers, HV-side sensors, and filter capacitor, are eliminated.

References

[1] International Energy Agency, *Global EV Outlook 2020*. France, Paris: IEA Publications, 2020. [Online]. Available: https://webstor e.iea

[2] Mobility Foresights, "Global electric vehicle on-board charger market 2019-2025," 2019. [Online]. Available: https://mobilityforesigh ts.com/product/global-electric-vehicle-on-board-charger-market/

[3] Y. Yan, H. Bai, A. Foote, and W. Wang, "Securing full-power-range zero-voltage switching in both steady-state and transient operations for a dual-active-bridge-based bidirectional electric vehicle charger," *IEEE Trans. Power Electron.*, vol. 35, no. 7, pp. 7506–7519, Jul. 2020.

[4] J. Park, M. Kim, and S. Choi, "Fixed frequency series loaded resonant converter based battery charger which is insensitive to resonant component tolerances," in *Proc. 7th Int. Power Electron. Motion Control Conf.*, Harbin, China, 2012, pp. 918–922.

[5] H. Wang, S. Dusmez, and A. Khaligh, "Maximum efficiency point tracking technique for LLC-based PEV chargers through variable DC link control," *IEEE Trans. Ind. Electron.*, vol. 61, no. 11, pp. 6041–6049, Nov. 2014.

[6] B. Li, F. C. Lee, Q. Li, and Z. Liu, "Bi-directional on-board charger architecture and control for achieving ultra-high efficiency with wide battery voltage range," in *Proc. IEEE Appl. Power Electron. Conf. Expo.*, Tampa, FL, USA, 2017, pp. 3688–3694.

[7] M. Kwon and S. Choi, "An electrolytic capacitorless bidirectional EV charger for V2G and V2H applications," *IEEE Trans. Power Electron.*, vol. 32, no. 9, pp. 6792–6799, Sep. 2017.

[8] H. Belkamel, K. Hyungjin, K. Beywongwoo, Y. Shin, and S. Choi, "Bi-directional single-stage interleaved totem-pole AC-DC converter with high frequency isolation for on-board EV charger," in *Proc. IEEE Energy Convers. Congr. Expo.*, Portland, OR, USA, 2018, pp. 6721–6724.

[9] S. Kim, A. M. Naradhipa, and S. Choi, "Development of a high power density GaN-based transistor low-voltage high-current phase-shift full-bridge current doubler converter for electric vehicles," in *Proc. IEEE Energy Convers. Congr. Expo.*, Baltimore, MD, USA, 2019, pp. 1364–1369.

[10] A. M. Naradhipa *et al.*, "A compact 700kHz 1.8kW GaN-based transistor low voltage high current DC-DC converter for xEV using planar matrix transformer," in *Proc. 10th Int. Conf. Power Electron. ECCE Asia)*, Busan, South Korea, 2019, pp. 1–6.

[11] B. Kim, K. Kim, and S. Choi, "A 800V/14V soft-switched converter with low-voltage rating of switch for xEV applications," in *Proc. Int. Power Electron. Conf. ECCE Asia)*, Niigata, Japan, 2018, pp. 256–260.

[12] F. Krismer and J. W. Kolar, "Efficiency-optimized high-current dual active bridge converter for automotive applications," *IEEE Trans. Ind. Electron.*, vol. 59, no. 7, pp. 2745–2760, Jul. 2012.

[13] G. Yang, P. Dubus, and D. Sadarnac, "Double-phase high-efficiency, wide load range high-voltage/low-voltage LLC DC/DC converter for electric/hybrid vehicles," *IEEE Trans. Power Electron.*, vol. 30, no. 4, pp. 1876–1886, Apr. 2015.

[14] B. Khasawneh, M. Sabra, and M. Zohdy, "Novel operating mode for DC-to-DC converters in PHEVs," SAE Int., Warrendale, PA, USA, SAE Tech. Paper 2013-01-1761, 2013.

[15] A. Khaligh and M. D'Antonio, "Global trends in high-power on-board chargers for electric vehicles," *IEEE Trans. Veh. Technol.*, vol. 68, no. 4, pp. 3306–3324, Apr. 2019.

[16] J. A. Baxter, D. A. Merced, D. J. Costinett, L. M. Tolbert, and B. Ozpineci, "Review of electrical architectures and power requirements for automated vehicles," in *Proc. IEEE Transp. Electrific. Conf. Expo.*, Long Beach, CA, USA, 2018, pp. 944–949.

[17] U.S. DRIVE Department of Energy, "Electrical and electronics technical team roadmap," Oct. 2017. [Online]. Available: https://www.energy.gov/sites/prod/files/2017/11/f39/EETT%20Roadmap%2010-27-17.pdf

[18] I. Subotic, N. Bodo, E. Levi, B. Dumnic, D. Milicevic, and V. Katic, "Overview of fast on-board integrated battery chargers for electric vehicles based on multiphase machines and power electronics," *IET Elect. Power Appl.*, vol. 10, no. 3, pp. 217–229, Mar. 2016.

[19] C. Shi and A. Khaligh, "A two-stage three-phase integrated charger for electric vehicles with dual cascaded control strategy," *IEEE J. Emerg. Sel. Topics Power Electron.*, vol. 6, no. 2, pp. 898–909, Jun. 2018.

[20] N. Sakr, D. Sadarnac, and A. Gascher, "A new combined bidirectional boost converter and battery charger for electric vehicles," in *Proc. 41st Annu. Conf. IEEE Ind. Electron. Soc.*, Yokohama, Japan, 2015, pp. 1258–1263.

[21] Y. Lee, A. Khaligh, and A. Emadi, "Advanced integrated bidirectional AC/DC and DC/DC converter for plug-in hybrid electric vehicles," *IEEE Trans. Veh. Technol.*, vol. 58, no. 8, pp. 3970–3980, Oct. 2009.
[22] BorgWarner, "OBC + APM package integrated charger," 2019. [Online]. Available: https://www.borgwarner.com/newsroom/press-releases/2019/05/16/class-leading-onboard-battery-charger-strengthens-borgwarner-s-ev-systems-leadership
[23] J. G. Pinto, V. Monteiro, H. Gonçalves, and J. L. Afonso, "Onboard reconfigurable battery charger for electric vehicles with traction-to-auxiliary mode," *IEEE Trans. Veh. Technol.*, vol. 63, no. 3, pp. 1104–1116, Mar. 2014.
[24] S. Kim and F. Kang, "Multifunctional onboard battery charger for plug-in electric vehicles," *IEEE Trans. Ind. Electron.*, vol. 62, no. 6, pp. 3460–3472, Jun. 2015.
[25] D. Kim, M. Kim, and B. Lee, "An integrated battery charger with high power density and efficiency for electric vehicles," *IEEE Trans. Power Electron.*, vol. 32, no. 6, pp. 4553–4565, Jun. 2017.
[26] H. V. Nguyen, D. To, and D. Lee, "Onboard battery chargers for plug-in electric vehicles with dual functional circuit for low-voltage battery charging and active power decoupling," *IEEE Access*, vol. 6, pp. 70212–70222, 2018.
[27] R. Hou and A. Emadi, "A primary full-integrated active filter auxiliary power module in electrified vehicles with single-phase onboard chargers," *IEEE Trans. Power Electron.*, vol. 32, no. 11, pp. 8393–8405, Nov. 2017.
[28] I. Aghabali, J. Bauman, and A. Emadi, "Analysis of auxiliary power unit and charging for an 800V electric vehicle," in *Proc. IEEE Transp. Electrific. Conf. Expo.*, Detroit, MI, USA, 2019, pp. 1–6.
[29] C. Liu *et al.*, "High-efficiency hybrid full-bridge–half-bridge converter with shared ZVS lagging leg and dual outputs in series," *IEEE Trans. Power Electron.*, vol. 28, no. 2, pp. 849–861, Feb. 2013.
[30] H. Ma, Y. Tan, L. Du, X. Han, and J. Ji, "An integrated design of power converters for electric vehicles," *Proc. IEEE 26th Int. Symp. Ind. Electron.*, Edinburgh, U.K., 2017, pp. 600–605.
[31] Y. Kim, C. Oh, W. Sung, and B. K. Lee, "Topology and control scheme of OBC–LDC integrated power unit for electric vehicles," *IEEE Trans. Power Electron.*, vol. 32, no. 3, pp. 1731–1743, Mar. 2017.
[32] Y. Tang, J. Lu, B. Wu, S. Zou, W. Ding, and A. Khaligh, "An integrated dual-output isolated converter for plug-in electric vehicles," *IEEE Trans. Veh. Technol.*, vol. 67, no. 2, pp. 966–976, Feb. 2018.
[33] G. Su and L. Tang, "A new integrated onboard charger and accessory power converter for plug-in electric vehicles," in *Proc. IEEE Energy Convers. Congr. Expo.*, Pittsburgh, PA, USA, 2014, pp. 4790–4796.

Gibum Yu (Student Member, IEEE) received the B.S. and M.S. degrees in control and instrumentation engineering from the Seoul National University of Science and Technology (Seoul Tech), Seoul, South Korea, in 2019 and 2021, respectively.

His research interests include power conversion technologies for renewable energy systems and electric vehicles.

Sewan Choi (Fellow, IEEE) received the Ph.D. degree in electrical engineering from Texas A&M University, College Station, TX, USA, in 1995.

From 1985 to 1990, he was with Daewoo Heavy Industries as a Research Engineer. From 1996 to 1997, he was a Principal Research Engineer with Samsung Electro-Mechanics Co., South Korea. In 1997, he joined the Department of Electrical and Information Engineering, Seoul National University of Science and Technology (Seoul Tech), Seoul, South Korea, where he is currently a Professor. He is President of Korean Institute of Power Electronics in 2021. His research interests include power conversion technologies for renewable energy systems and dc–dc converters and battery chargers for electric vehicles.

Dr. Choi has been serving as an Associate Editor of the IEEE TRANSACTIONS ON POWER ELECTRONICS since 2006. He was TPC chair of ICPE2019-IEEE ECCE Asia held in Busan, Korea. He is currently serving as Chairman of IEEE PELS Seoul section.